

## EFFECTS OF SPATIAL ENERGY DISTRIBUTION ON DEFECTS AND FRACTURE OF LPBF 316L STAINLESS STEEL

Elliott Jost<sup>\*,†</sup>, John Miers<sup>\*,†</sup>, Aron Robinson<sup>†</sup>, David Moore<sup>†</sup>, Christopher Saldana<sup>\*</sup>

<sup>\*</sup>George W. Woodruff School of Mechanical Engineering, Georgia Institute of Technology,  
Atlanta, GA 30332

<sup>†</sup>Sandia National Laboratories, Albuquerque, NM 87123

### Abstract

Measures of energy input and spatial energy distribution during laser powder bed fusion additive manufacturing have significant implications for the build quality of parts, specifically relating to formation of internal defects during processing. In this study, scanning electron microscopy was leveraged to investigate the effects of these distributions on the mechanical performance of parts manufactured using laser powder bed fusion as seen through the fracture surfaces resulting from uniaxial tensile testing. Variation in spatial energy density is shown to manifest in differences in defect morphology and mechanical properties. Computed tomography and scanning electron microscopy inspections revealed significant evidence of porosity acting as failure mechanisms in printed parts. These results establish an improved understanding of the effects of spatial energy distributions in laser powder bed fusion on mechanical performance.

### Introduction

Additive manufacturing (AM), the layer-by-layer buildup of a 3D component based on a digital model, offers significant advantages over traditional manufacturing techniques in terms of cost-to-complexity ratio as well as time and cost for small batches of parts [1]. However, along with these advantages comes the difficulty of safely implementing AM components in high-consequence applications, such as for rotating engine blades where the internal defect structure of AM components must be tightly controlled. Consequently, qualification, the determination of the integrity of a component, has become an increasingly important subject of interest in the research community [2–5]. In-situ monitoring and computed tomography are used to determine part integrity in-situ (during the build process) and post-build, respectively [5].

In the present study, comparisons were made between measures of global energy density (GED), mechanical properties, and quantitative scanning electron microscopy fractography measurements of 316L stainless steel tensile samples printed using three separate GED conditions. The goal of this study is to elucidate the effects of processing defects as they relate to the mechanical properties of laser powder bed fusion (LPBF) parts printed using various laser powers at constant laser speed and hatch spacing.

### **Qualification**

In-situ monitoring of the printing process is often used in qualification efforts in large part due to its potential to determine defect formation during a build and its potential use for implementing feedback control of the AM process. In-situ corrections of process parameters can

be used to create so-called “born qualified” parts that are determined to meet a final specification as soon as they are removed from the build plate [6]. Craeghs et al. [7] successfully demonstrated the use of optical sensors to implement feedback control during the printing process for surface roughness improvement. In their review, Spears and Gold [8] identified over 50 process parameters relating to the laser, stock powder, powder bed properties, recoating, and build environment that influence the final part quality for a variety of metal material systems, highlighting the difficulty of using in-situ monitoring for qualification.

In addition to in-situ monitoring, microcomputed tomography (CT) has been an effective research tool for the inspection and characterization of AM parts due to its ability to nondestructively take high resolution 2D images and reconstruct them to create 3D volumetric data. This data can be used to visualize defect location and morphology within AM-produced components. Other methods of inspection such as serial sectioning [9] can be used to inspect parts, but at the expense of a significant time investment and the destruction of the sample. Kim et al. [10] developed 3D image processing techniques to improve the reliability of CT data analysis and also attempted to standardize these methods using CoCr parts. In another study, Kim et al. [11] used CT to directly inspect internal defects of Inconel 625 AM parts. In an extensive review on the use of CT for AM inspection, Thompson et al. [12] discusses the advantages of using CT inspection to measure pore morphology, location, and distribution. Synchrotron CT has also been employed to quantify processing defects in AM parts on the sub-micron scale [13]. Moreover, several studies have utilized CT to understand the conditions under which defects are created across a variety of material systems including 316L, Ti-6Al-4V, and 304L stainless steel [14–16].

### **Correlation of Defects and Mechanical Properties**

To qualify a component, one must first understand the effects of defects and features of interest and the degree to which these defects and features will impact part performance, which is the motivation of this study. Only then can a determination be made as to the integrity of a part. A variety of studies have been performed in order to elucidate the complex relationship between defects and performance in AM parts across a variety of metals [17–22]. However, few of these studies consider or provide quantitative metrics on porosity morphology in attempt to relate defects to properties. Recently, efforts have been made to understand how pore morphology data can be used to understand the role of defects as stress concentrators [23].

In a study on the effects of non-optimum energy density in Ti-6Al-4V AM components, Gong et al. [17] concluded that low-energy density input was more detrimental to part performance than high-energy density input. Madison et al. [18] found that there was little correlation between metrics such as total defect volume or number of defects and properties in 304L stainless steel. Carlton et al. [19], using synchrotron radiography, found that voids can act as crack initiation sites and that effects were most significant in samples with nonuniform defect distributions in 316L. It is important to note that while the above studies cover a variety of materials and, as such, their findings cannot be directly applied to 316L stainless steel, their collective conclusions are helpful for understanding the role of defects AM components in general. Through correlation of pore morphology metrics obtained using SEM images and part

mechanical properties, this paper aims to provide insight into the defect-property relationship in efforts to standardize the qualification of AM components.

## Methods

### Manufacture

In the present study, three tensile test sample arrays (75 total samples), CT scans of which are presented in Figure 1a, were printed with an EOS M 290 LPBF machine equipped with a 400W IPG Photonics Laser using 316L stainless steel powder with a nominal particle size distribution of 30-60  $\mu\text{m}$ .

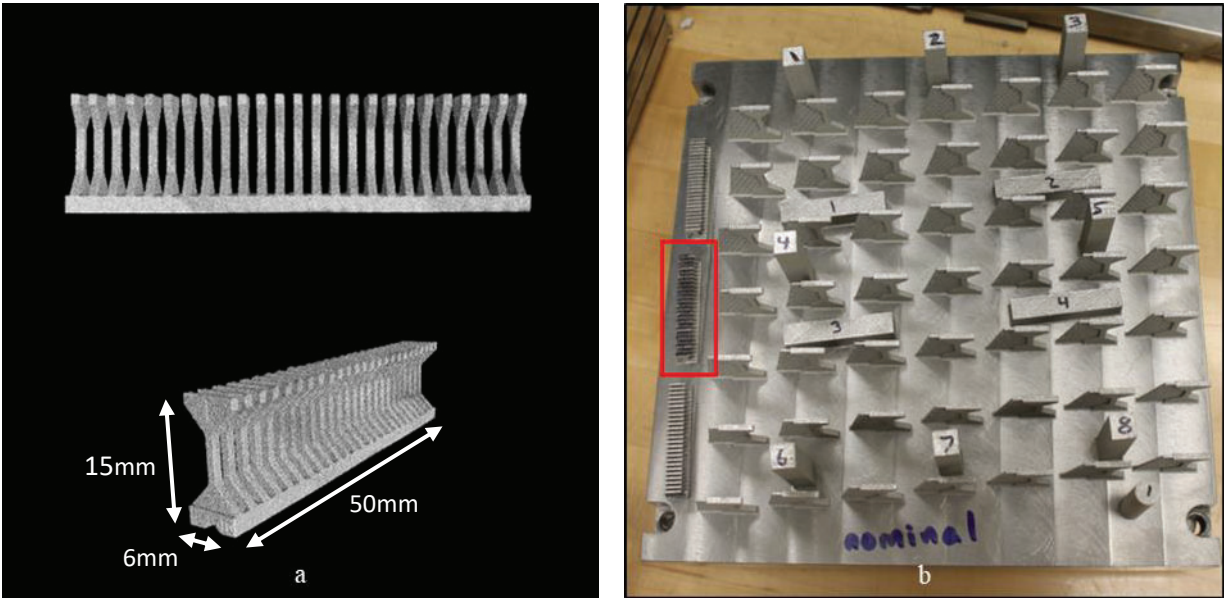


Figure 1. a) CT images of As-Built Sample Array b) Photo of the Nominal Build Plate with Analyzed Set Highlighted. Wiper direction is top-to-bottom and Argon flow is from right-to-left.

Three build plates containing a variety of parts were printed at three different global energy distribution (GED) levels that will be referred to as high, nominal, and low GED levels. One sample array set was analyzed from each build plate, the build plate location of which is highlighted in Figure 1b. GED, a measure of laser energy input per area [1], can be calculated using Eq. 1, below,

$$GED = \frac{P}{H S} \quad (1)$$

where  $P$  is laser power,  $H$  is hatch spacing, and  $S$  is laser speed. GED is the spatial equivalent of volumetric energy density [1]. In this study, GED was altered by changing the laser power while maintaining constant hatch spacing and laser speed values. GED parameters used in this study are shown in Table 1.

Table 1. Global Energy Distribution Parameters

	P (W)	H (mm)	S (mm/s)	GED (J/mm <sup>2</sup> )
<b>High GED</b>	220	0.09	1083	2.26
<b>Nominal GED</b>	195	0.09	1083	2.00
<b>Low GED</b>	170	0.09	1083	1.74

## Computed Tomography Inspection

Prior to mechanical testing, all samples were nondestructively inspected using a Nikon M2 Dual Head 225/450 kV computed tomography system. Samples were inspected at 440 kV and 227  $\mu$ A while using a 1 mm Cu filter to mitigate beam hardening image artifacts caused by the naturally polychromatic energy output of laboratory x-ray sources. Helical scanning was employed to effectively remove some types of image artifacts while allowing single-scan data acquisition of each of the elongated samples used in this study. To mitigate the interference of circular artifacts with data processing techniques, an off-axis center of rotation was used, which can create higher resolution scans but is prone to introducing additional noise and streaking. A resolution of  $\sim 10$   $\mu$ m/voxel was achieved using a Perkin Elmer detector and 2294 projections with 8 frames averaged per projection. Total CT inspection time was approximately 2 hours per array. Reconstruction and porosity analysis were performed using Nikon Metrology X-Tek CT Pro 3D and Volume Graphics VGSTUDIO MAX 3.2<sup>TM</sup>, respectively.

The scanned sample arrays were initially segmented using an ISO-50 threshold followed by an advanced surface refinement using a deformable surface technique for a more accurate determination of surface contours. Additionally, noise particles and voids were removed in this process. Following segmentation, planes were fit to the top, right, and front surfaces of each array. Each volume was then digitally registered such that the top plane normal vector is used as the direction for the positive z-axis, the line formed by the intersection of the top and right planes is used for the direction of the x-axis, and the point where all three fit planes intersect is set as the origin of the coordinate system. Plane fit points and the defined coordinate system are shown in green and red in Figure 2a, respectively.

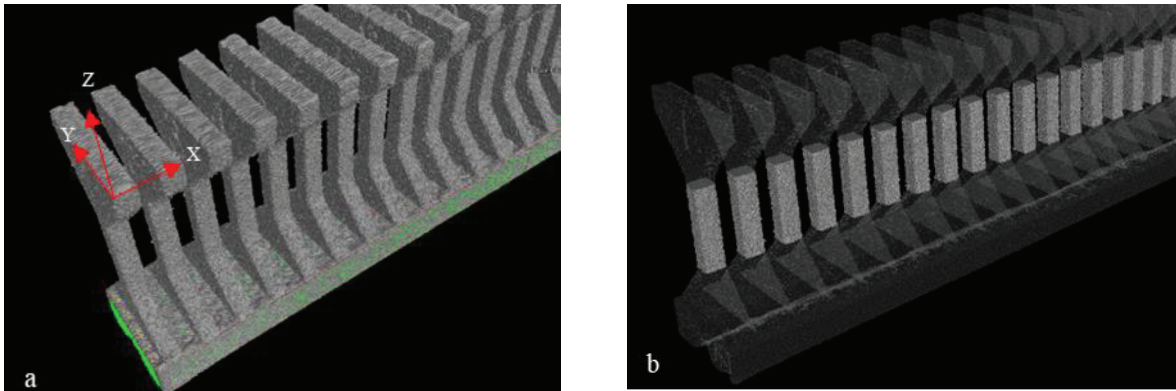


Figure 2. Example fit points (colored dots) used to digitally register each object volume. a.) Fit points shown in green on volume. b.) Opaque gage regions with 85% transparent sample array.

The gage region of each tensile sample in each array was isolated for individual porosity assessment. Since the as-designed dimensions and distribution of the specimens was the same across all arrays examined in the present work, the coordinate system defined above allows for the use of uniform parameters in the definition of the regions of interest for consistent comparison between datasets. To separate the gage region of each tensile sample, a rectangular cuboid region of interest (ROI) was created. A Boolean intersection of this ROI with the segmented material was then performed to obtain a single unified ROI that encompasses the exact contours of the gage regions. Gage regions of the sample array are visualized as opaque in Figure 2b.

Finally, porosity in each gage region was identified using VGDefX™, a built-in porosity analysis tool of VGSTUDIO MAX 3.2. A medium adaptive noise reduction was used along with a 2-voxel offset from the determined surface to clean up the material inside the gage region. Results of the porosity analysis were filtered to only include pores with realistic void shape. Table 2 contains the filter parameters that the identified porosity had to fall within to be considered real. The probability threshold does not represent a percentage, but rather a numerical value assigned to each pore that is the assessment of an internal weighted function in VGDefX™. Compactness is the ratio of pore's volume to that of a circumscribed sphere of the same diameter. Similarly, sphericity is the ratio of a pore's surface to that of its circumscribed sphere.

*Table 2. Parameters used to filter the results of the porosity analysis in VGDefX™ of VGSTUDIO MAX 3.2.*

Probability Threshold	Effective Pore Diameter [mm]	Compactness	Sphericity
>0.85	0.0625-1.00	0.08-1.00	0.13-0.65

Through CT inspection, it was found that the high GED samples contained high individual pore volume with a moderate number of pores within the gage volume, nominal GED samples had small individual pore volume and a low number of pores, and low GED samples contained small individual pore volume with a large number of pores. Most importantly, porosity distributions were found to be spatially uniform along the z-axis of the gage region, suggesting that fracture surface SEM inspections fairly sample the porosity distributions. CT porosity measurements were found to agree with SEM fracture surface inspection measurements. Quantitative porosity metrics will be presented later in this paper.

## **High-Throughput Mechanical Testing**

An automated high-throughput tensile testing procedure was developed to test tensile bars for rapid characterization of mechanical properties of AM samples. Tensile testing was accomplished using an MTS servo-hydraulic load frame equipped with an Interface 2-kip load cell and a mounting stage for sample movement. Sample were moved using screw-driven linear motion with a KeLing Technologies, Inc. stepper motor and a Temposonics® position sensor. Real-time DIC strain tracking using VIC-Gauge™ software by Correlated Solutions allowed for further automation by using non-contact strain measurements to reduce the need for operator intervention. Two cameras, normal to the front and right faces of each sample, were used for strain tracking cross sectional area measurements. A pixel-to-millimeter ratio was established

using a reference image of known dimensions and applied to the first photo taken of every sample to determine the initial area using a MATLAB algorithm. Samples were speckled with a white undercoat and black speckle pattern via spray paint and pulled at a constant rate of 0.03 mm/s. A MATLAB code was written to process the data and create stress-strain curves as well as generate a results file listing the yield strength at 0.2% offset, ultimate tensile strength, uniform elongation, and the strain to failure for each individual specimen.

### Scanning Electron Microscopy Inspection

Following tensile testing, a Zeiss Ultra 60 Field Emission Scanning Electron Microscope (SEM) equipped with a Schottky FEG gun was used to image the 150 fracture surfaces resulting from tensile testing. Samples were imaged at a working distance of approximately 8 mm and an acceleration voltage of 15 kV using the secondary electron detector to accurately capture topographical information of the fracture surfaces. Samples 1, 5, 13, 21, and 25 were selected as samples of interest from each sample array, as seen in Figure 3, and subjected to closer SEM inspection to determine if fractographic differences existed between samples produced on the edges and middle of the samples, as detailed below.

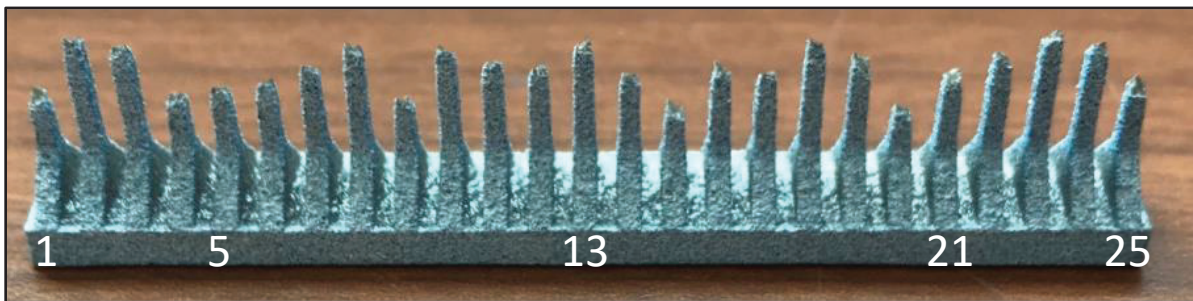


Figure 3. Post-fracture image of sample array. Samples 1 to 25 shown left to right. Dimensions shown in Figure 1a.

### Quantitative Fractography

FIJI, an ImageJ analysis package [24], was used to quantitatively inspect porosity observed on the fracture surfaces of the analyzed samples. The samples of interest were analyzed quantitatively from each sample array using an SEM image containing the entire fracture surface at  $\sim 250\times$  magnification and a resolution of  $\sim 3\mu\text{m}/\text{pixel}$ . Using the freehand selection tool, 647 pores were manually identified across these 15 samples by tracing the outside edge of each pore. Only bottom fracture surfaces, or those still attached to the array as seen in Figure 3 were analyzed quantitatively, as the complimentary fracture surfaces were assumed to be identical for the purposes of this study. Porosity metrics calculated from image analysis include pore area, Feret (longest) diameter, centroid, circularity, as well as distance between pore centroid and fracture surface centroid. An example of pore identification can be seen in Figure 4.

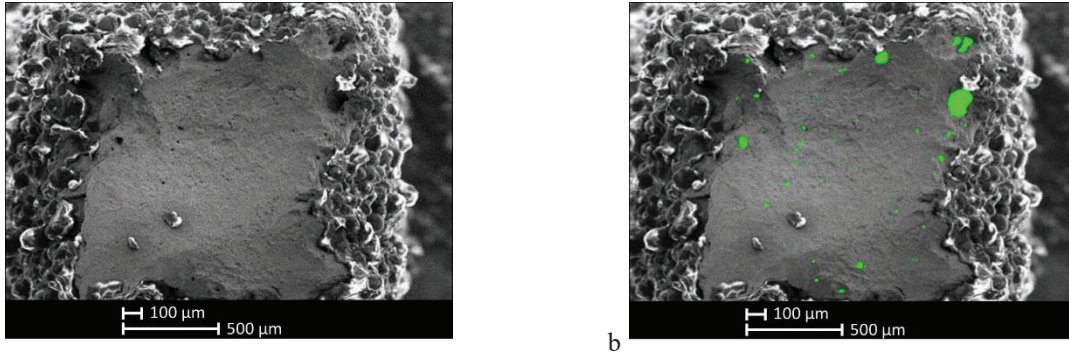


Figure 4. a) Original SEM image of N13. b) SEM with analyzed pores highlighted in green.

A variety of sizes and shapes of pores were identified on the fracture surfaces. As will later be shown quantitatively, the largest pores tended to cluster around the edges of the samples, as exemplified in Figure 4 and Figure 5. Figure 5 shows several of the analyzed samples in a visual summary of the porosity found during the quantitative fractography analysis where analyzed pores are segmented in green. In Figure 5 it can be seen that defects observed by SEM are larger in the high GED samples and significantly smaller, on average, in the low GED samples. Because the focus of this study is internal porosity and not the tortuous surface “crust” heterogeneities detailed in other studies [25], only pores that were determined to be completely internal as seen from SEM imaging were included for analysis.

	Sample 1	Sample 13	Sample 25
High GED			
Nominal GED			
Low GED			

Figure 5. Visual Summary of Select Analyzed Samples.

## Results and Discussion

### Comparison of Porosity Metrics to Energy Density

From the collected quantitative fractography data, comparisons were made between porosity metrics and GED to understand the effect that energy input has on porosity formation in 316L stainless steel AM components. Figure 6 shows comparisons of mean pore area and GED, which reveals a clear trend where high, nominal, and low GED samples have mean areas of 140.2  $\mu\text{m}^2$ , 67.5  $\mu\text{m}^2$ , and 32.6  $\mu\text{m}^2$ , respectively. Figure 6b shows the mean area of the five largest pores on each inspected sample and shows a similar trend, with high, nominal, and low pore sizes of 800.9  $\mu\text{m}^2$ , 400.4  $\mu\text{m}^2$ , and 144.6  $\mu\text{m}^2$ . The five largest pores seen on each fracture surface are considered in this and other figures to understand whether a minimum critical defect size that impacts mechanical performance can be determined for establishing inspection specifications. Defect size distributions were found to be non-Gaussian due to the extreme outliers in high and nominal GED samples and thus trends should not scale linearly as a result of Gaussian distribution sampling properties but rather due to the dominating effects of the largest defects.

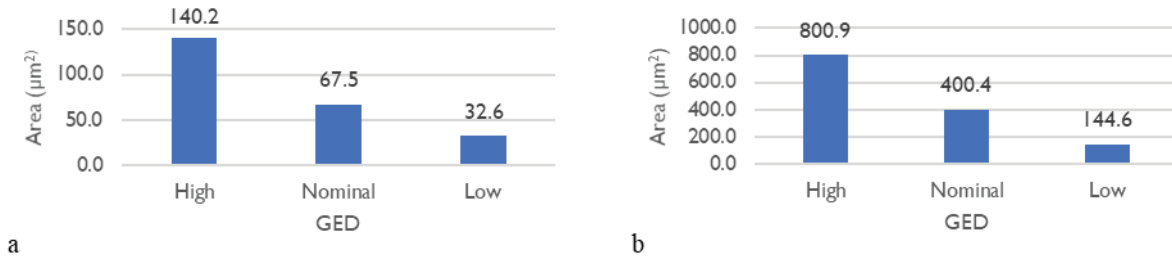


Figure 6. a) Average Sample Pore Area vs. GED. b) 5 Largest Pores Mean Area vs. GED.

In addition to pore area, distance between each pore's 2D centroid and the 2D centroid of the fracture surface, defined as the center of the gage cross-section, was calculated. These results are presented in Figure 7. As shown, the average distance of the pore from the part center is greatest in the high GED samples and smallest in the low GED samples, indicating that pores exist farther from the center in high GED samples, regardless of size. This trend is even more severe when only considering the five largest pores from each sample where the average distance of the largest five pores is more than four times larger in the high GED than low GED samples. Due to necking behavior observed in the samples, the maximum possible distance is less than 375  $\mu\text{m}$ , half the nominal specimen width, and is estimated to be approximately 325  $\mu\text{m}$ .

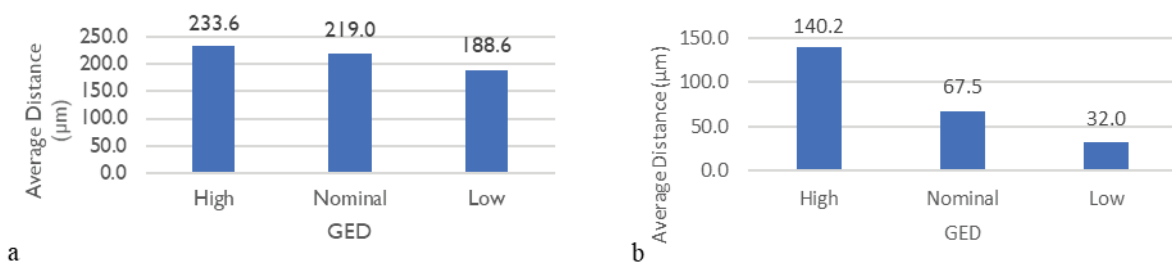


Figure 7. a) Pore Center to Part Center Distance vs. GED. b) Biggest 5 Pores Pore Center to Part Center Distance vs. GED

Figure 8 provides a visual representation of pore location and pore distance to part center and shows the 2D location of each pore for each GED type, where location (0,0) is the center of each part and the black rectangle represents the nominal edges of the sample. The reader should note that the circles in Figure 8 are shown for the purposes of representing the location and relative size of the pores using the pore area calculated during SEM inspection and should not be interpreted as an absolute representation of pore size or shape. Figure 8d shows the locations of pores with areas in at least the 95<sup>th</sup> percentile, most of which occur near the edge of the part. Note that in the distribution of the 33 pores in this percentile range, 21 are in the high GED samples, 11 in the nominal GED, and 1 in the low GED. The authors note that pores shown in Figure 8d are primarily concentrated in the upper part of the plot and hypothesize that the cause of this may be due to the part location on the build plate as well as the flow of the inert gas in the build chamber. Further investigation is needed to draw more concrete conclusions.

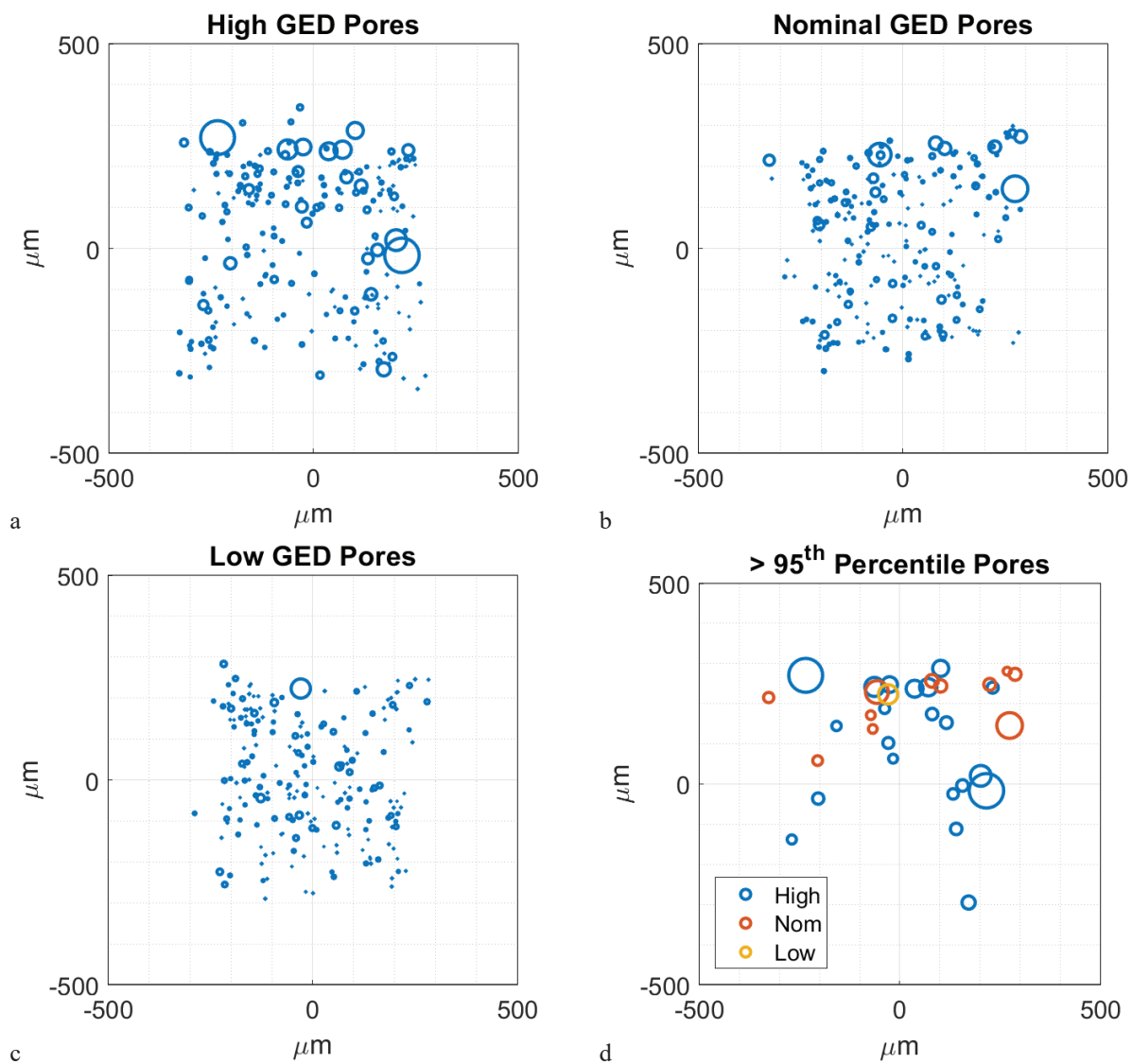


Figure 8. Pore Location Maps. a) High b) Nominal c) Low GED Condition Pores. d) Pores in 95<sup>th</sup> percentile or above volumetrically.

Based on the results displayed in Figure 6, Figure 7, and Figure 8, it is hypothesized that the cause of the increase in the number of large pores as well as their location near the edge of the specimens is due to the path of the laser. It is well-established that the likelihood of keyhole porosity formation is increased in laser welding and SLS of stainless steels when energy input is elevated [14–16]. It is plausible that the raster pattern used in the printing of these samples resulted in a non-optimal energy input at the points at which the laser reverses directions on the sample. The instantaneous zero-velocity of the laser can result in a momentary elevation of energy input and cause the formation of keyhole porosity. In the nominal GED samples, perturbations in laser power and control parameters could have resulted in an increased likelihood of either keyhole porosity formation or lack of fusion around the edges of the samples. In the high GED samples, the increased laser power in addition to the parameter perturbations likely caused the frequent keyhole porosity observed in the SEM inspections of the fracture surfaces.

Conversely, the low GED samples did not have sufficient energy input to cause keyholing to occur. Keyhole formation has been linked to normalized enthalpy thresholds, above which keyhole mode melt pool formation dominates over the preferred conduction mode [14]. It is hypothesized that the low GED samples did not exceed the normalized enthalpy threshold for 316L stainless steel, and thus did not experience keyhole porosity formation. Gas porosity, however, formed by the entrapment of inert gas flowing in the build chamber, is commonly small and spherical in shape, as seen in the low GED samples. Shape of porosity can be used to distinguish between gas pores and lack of fusion pores, which are common when there is insufficient energy input to completely fuse powders together, resulting in a random pore shape rather than a spherical pore shape. Due to the low number of large pores in Low GED samples, it is hypothesized that the small pores observed in these samples as well as their relatively uniform spatial distribution across the examined fracture surfaces of all samples are likely gas and lack of fusion porosity.

### Comparison of Mechanical Properties to Porosity Metrics

Comparisons were made between the mechanical properties of the and porosity metrics of the SEM-inspected samples to elucidate the complex relationship between defects and final mechanical properties. Several mechanical properties were measured from tensile test data including ultimate tensile strength (UTS), ductility, and yield stress. Average measured mechanical properties of all 75 samples are shown compared to GED in Figure 9 and to wrought and annealed 316L stainless steel properties in Table 3.

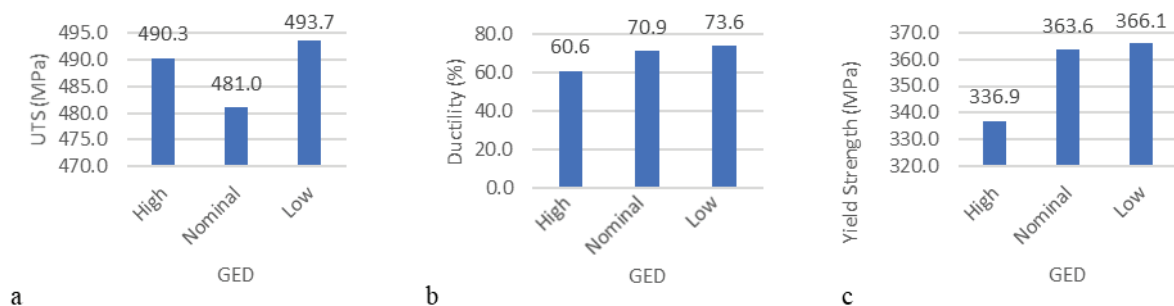


Figure 9. Mechanical Properties of all Samples vs. GED. a) UTS. b) Ductility. c) Yield Strength.

Table 3. Summary of Analyzed Sample Properties of all Samples  $\pm 1$  Standard Deviation and Wrought and Annealed 316L Properties [26]

	UTS (MPa)	Ductility (%)	Yield Strength (MPa)
High GED	490.3 $\pm$ 12.34	60.6 $\pm$ 3.99	336.9 $\pm$ 20.96
Nominal GED	481.0 $\pm$ 9.66	70.9 $\pm$ 4.62	363.6 $\pm$ 7.66
Low GED	493.7 $\pm$ 7.28	73.6 $\pm$ 4.53	366.1 $\pm$ 12.90
Wrought + Annealed	515	60	205

As can be seen in Figure 9, mechanical properties can vary significantly with GED type. Most significantly, ductility was found to vary greatly with increased GED, as evidenced by the poor performance of the high GED samples at 60.6% compared to 73.6% in the low GED samples, as shown in Figure 9b. UTS and yield strength also varied with GED type, with high samples performing well for UTS at 490.3 MPa and poorly for yield strength at 336.9 MPa. However, most important to consider is how these properties vary based on defect metrics such that a minimum critical defect size can be established. As seen in Figure 10a and Figure 10b, pore area seems to have no significant correlation with ultimate tensile strength based on the wide spread of intra-array UTS performance, even in the nominal GED samples.

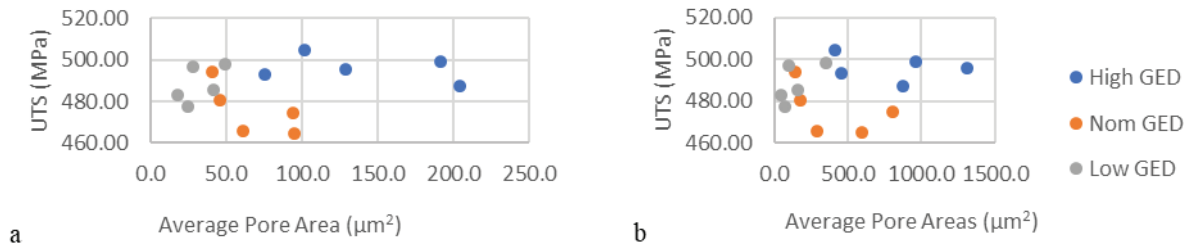


Figure 10. UTS vs. Pore Area. a) All Pores. b) Top 5 Largest Pores Per Sample

Figure 11a and Figure 11b reveal that pore area plays a significant role in the ductility of samples by showing a negative linear trend between ductility and average pore area. Perhaps most interestingly, ductility seems to be uniformly affected by mean pore area as well as the area of the 5 largest pores. The persistence of this trend when only considering the largest pores suggests that the largest pores dominate effects on performance and that it may be sufficient to only consider these pores for component inspection and qualification. Because the largest pores on the fracture surface seem to dominate ductility performance, pore size thresholds can be intelligently determined to inform the inspection process.

Furthermore, there exists a negative trend between ductility and pore distance to center as shown in Figure 11c. Because necking occurred less in the low ductility samples, it is difficult to determine whether the observed trend is due to the natural movement inward of the pores during the necking process or whether there is a true correlation between ductility and pore location. Pre-mechanical testing inspection such as computed tomography could be used to avoid this necking effect on inspection.

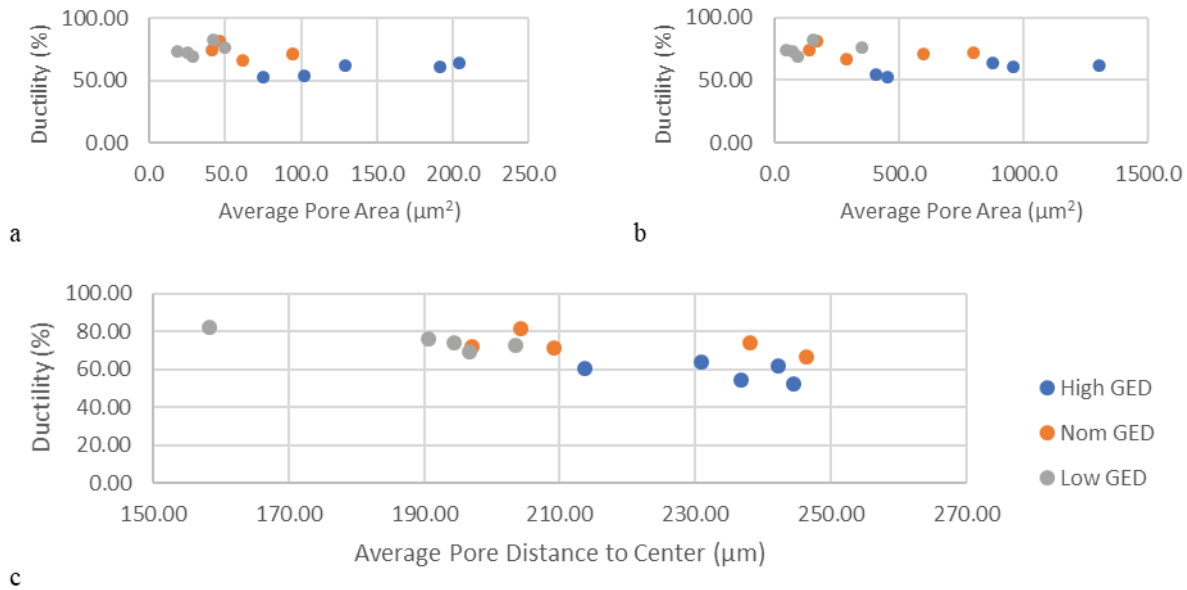


Figure 11. Ductility vs. Pore Morphology. a) Pore Area. b) Top 5 Pore Area. c) Pore Distance to Center

Shown in Figure 12 is the relationship between yield strength and pore area. Similar to the ductility vs pore area relationship, a negative linear trend is observed between these two variables. Additionally, this trend of decreasing property value with increasing pore area is preserved even when considering only the five largest pores, again showing the dominating effect of the largest pores.

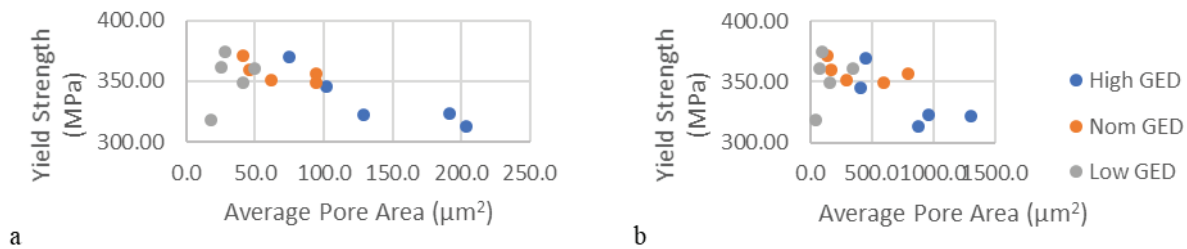


Figure 12. Yield Strength vs. Pore Area. a) All Pores. b) Top 5 Pores.

The dominating effect of the largest pores of a fracture surface on the mechanical performance of a component in terms of ductility and yield strength are significant findings for the progress towards AM part qualification. Relationships presented in this study suggest that defect impact on mechanical performance is governed only by defects in excess of some critical size. The determination of minimum critical defect sizes for various loading applications will result in establishment of inspection routines that are capable of adequately inspecting components for critical flaws as well as optimized for time, cost, and complexity of inspection.

Although the data presented in this study indicates that only the largest pores at the fracture surface matter, it is unclear, due to the geometrically-identical specimens tested, how

these effects may vary with part size, geometry, or loading condition. Thus, it is unclear whether inspection criteria should be established based on a universal minimum defect size or whether the pore size-to-stressed area ratio is the determining factor in influencing part performance. Further studies will need to be performed to make the influence of these competing factors clear for the eventual establishment of inspection criteria for AM components.

### **Conclusion**

In this study, experiments and inspections were performed to correlate mechanical performance of AM tensile samples to defects observed and measured through scanning electron microscopy. Computed tomography was used for bulk inspection of components and determination of whole-part defect metric distributions. SEM inspections and image analysis tools were used to measure morphology and location metrics of defects present on the fracture surfaces of samples at resolutions higher than that of CT. From the correlation of mechanical performance and defect metrics, the following conclusions can be made.

1. Mechanical properties of AM 316L stainless steel are influenced by fluctuations in global energy density varied by laser power. Non-optimal energy input density results in the deterioration of mechanical performance as measured by ductility and yield strength.
2. Higher-than-prescribed energy input density is more detrimental to AM 316L stainless steel part performance than is lower-than-prescribed energy input density at the levels tested due to keyhole porosity formed by high energy input.
3. When only considering the largest pores observed on a fracture surface, all relationships between pore morphology and mechanical properties found in this study were preserved, indicating the dominating effect of the largest pores on part performance.

This work establishes a direct relationship between large, keyhole porosity and decreased mechanical performance, however further investigation is necessary to thoroughly understand this relationship. Further work to understand the defect-property-performance relationship includes determining how the pore-to-stressed area ratio determines the effect of pores on global part performance, how the conclusions drawn from this study apply to more complex geometries and other materials, how microstructure affects performance, and establishment of minimum critical defect size thresholds for inspection of AM components. These studies will serve to understand the influence of defects on AM part performance and improve the usefulness and safety of additively manufactured components.

### **Acknowledgements**

Sandia National Laboratories is a multi-mission laboratory managed and operated by National Technology & Engineering Solutions of Sandia, LLC, a wholly owned subsidiary of Honeywell International, Inc., for the U.S. Department of Energy's National Nuclear Security Administration under contract DE-NA0003525.

This paper describes objective technical results and analysis. Any subjective views or opinions that might be expressed in the paper do not necessarily represent the views of the U.S. Department of Energy or the United States Government.

## References

- [1] DebRoy, T., Wei, H. L., Zuback, J. S., Mukherjee, T., Elmer, J. W., Milewski, J. O., Beese, A. M., Wilson-Heid, A., De, A., and Zhang, W., 2018, “Additive Manufacturing of Metallic Components – Process, Structure and Properties,” *Progress in Materials Science*, **92**, pp. 112–224.
- [2] Peralta, A. D., Enright, M., Megahed, M., Gong, J., Roybal, M., and Craig, J., 2016, “Towards Rapid Qualification of Powder-Bed Laser Additively Manufactured Parts,” *Integrating Materials and Manufacturing Innovation*, **5**(1).
- [3] Seifi, M., Gorelik, M., Waller, J., Hrabe, N., Shamsaei, N., Daniewicz, S., and Lewandowski, J. J., 2017, “Progress Towards Metal Additive Manufacturing Standardization to Support Qualification and Certification,” *JOM*, **69**(3), pp. 439–455.
- [4] Roach, R. A., Bishop, J. E., Johnson, K., Rodgers, T., Boyce, B. L., and Swiler, L., “Using Additive Manufacturing as a Pathway to Change the Qualification Paradigm,” p. 11.
- [5] Seifi, M., Salem, A., Beuth, J., Harrysson, O., and Lewandowski, J. J., 2016, “Overview of Materials Qualification Needs for Metal Additive Manufacturing,” *JOM*, **68**(3), pp. 747–764.
- [6] Roach, R. A., Abdeljawad, F., Argibay, N., Allen, K., Balch, D., Beghini, L., Bishop, J., Boyce, B., Brown, J., Burchard, R., Chandross, M., Cook, A., Dressler, A., Forrest, E., Ford, K., Ivanoff, T., Jared, B., Kammler, D., Koepke, J., Kustas, A., Lavin, J., Leathe, N., Lester, B., Madison, J., Mani, S., Martinez, M. J., Moser, D., Murphy, R., Rodgers, T., Seidl, T., Shaklee-Brown, H., Stanford, J., Stender, M., Sugar, J., Swiler, L. P., Taylor, S., Trembacki, B., Waanders, B. van B., Whetton, S., Wildey, T., and Wilson, M., “Born Qualified Grand Challenge LDRD Final Report,” p. 105.
- [7] Craeghs, T., Bechmann, F., Berumen, S., and Kruth, J.-P., 2010, “Feedback Control of Layerwise Laser Melting Using Optical Sensors,” *Physics Procedia*, **5**, pp. 505–514.
- [8] Spears, T. G., and Gold, S. A., 2016, “In-Process Sensing in Selective Laser Melting (SLM) Additive Manufacturing,” *Integrating Materials and Manufacturing Innovation*, **5**(1).
- [9] Uchic, M. D., Groeber, M. A., and Rollett, A. D., “Automated Serial Sectioning Methods for Rapid Collection of 3D Microstructure Data (Preprint),” p. 11.
- [10] Kim, F. H., Moylan, S. P., Garboczi, E. J., and Slotwinski, J. A., 2017, “Investigation of Pore Structure in Cobalt Chrome Additively Manufactured Parts Using X-Ray Computed Tomography and Three-Dimensional Image Analysis,” *Additive Manufacturing*, **17**, pp. 23–38.
- [11] Kim, F. H., Villarraga-Gómez, H., and Moylan, S. P., 2016, “Inspection of Embedded Internal Features in Additively Manufactured Metal Parts Using Metrological X-Ray Computed Tomography,” **64**, p. 6.
- [12] Thompson, A., Maskery, I., and Leach, R. K., 2016, “X-Ray Computed Tomography for Additive Manufacturing: A Review,” *Measurement Science and Technology*, **27**(7), p. 072001.
- [13] Cunningham, R., Narra, S. P., Montgomery, C., Beuth, J., and Rollett, A. D., 2017, “Synchrotron-Based X-Ray Microtomography Characterization of the Effect of Processing Variables on Porosity Formation in Laser Powder-Bed Additive Manufacturing of Ti-6Al-4V,” *JOM*, **69**(3), pp. 479–484.
- [14] King, W. E., 2014, “Observation of Keyhole-Mode Laser Melting in Laser Powder-Bed Fusion Additive Manufacturing,” *Journal of Materials Processing Technology*, p. 11.

- [15] Madison, J. D., and Aagesen, L. K., 2012, “Quantitative Characterization of Porosity in Laser Welds of Stainless Steel,” *Scripta Materialia*, **67**(9), pp. 783–786.
- [16] Martin, A. A., Calta, N. P., Khairallah, S. A., Wang, J., Depond, P. J., Fong, A. Y., Thampy, V., Guss, G. M., Kiss, A. M., Stone, K. H., Tassone, C. J., Nelson Weker, J., Toney, M. F., van Buuren, T., and Matthews, M. J., 2019, “Dynamics of Pore Formation During Laser Powder Bed Fusion Additive Manufacturing,” *Nat Commun*, **10**(1), p. 1987.
- [17] Gong, H., Rafi, K., Gu, H., Janaki Ram, G. D., Starr, T., and Stucker, B., 2015, “Influence of Defects on Mechanical Properties of Ti–6Al–4V Components Produced by Selective Laser Melting and Electron Beam Melting,” *Materials & Design*, **86**, pp. 545–554.
- [18] Madison, J. D., Underwood, O. D., Swiler, L. P., Boyce, B. L., Jared, B. H., Rodelas, J. M., and Salzbrenner, B. C., 2018, “Corroborating Tomographic Defect Metrics with Mechanical Response in an Additively Manufactured Precipitation-Hardened Stainless Steel,” Provo, Utah, USA, p. 020009.
- [19] Carlton, H. D., Haboub, A., Gallegos, G. F., Parkinson, D. Y., and MacDowell, A. A., 2016, “Damage Evolution and Failure Mechanisms in Additively Manufactured Stainless Steel,” *Materials Science and Engineering: A*, **651**, pp. 406–414.
- [20] Carlton, H. D., Klein, K. D., and Elmer, J. W., 2019, “Evolution of Microstructure and Mechanical Properties of Selective Laser Melted Ti-5Al-5V-5Mo-3Cr after Heat Treatments,” *Science and Technology of Welding and Joining*, pp. 1–9.
- [21] Sheridan, L., Scott-Emuakpor, O. E., George, T., and Gockel, J. E., 2018, “Relating Porosity to Fatigue Failure in Additively Manufactured Alloy 718,” *Materials Science and Engineering: A*, **727**, pp. 170–176.
- [22] Wauthle, R., Vrancken, B., Beynaerts, B., Jorissen, K., Schrooten, J., Kruth, J.-P., and Van Humbeeck, J., 2015, “Effects of Build Orientation and Heat Treatment on the Microstructure and Mechanical Properties of Selective Laser Melted Ti6Al4V Lattice Structures,” *Additive Manufacturing*, **5**, pp. 77–84.
- [23] Miers, J. C., Jost, E. W., Moore, D. G., Jared, B., and Salanda, C., 2019, “Effects of Pore Orientation and Shape on Failure in Additively Manufactured 316L SS,” Garden Grove, CA.
- [24] Schindelin, J., Arganda-Carreras, I., Frise, E., Kaynig, V., Longair, M., Pietzsch, T., Preibisch, S., Rueden, C., Saalfeld, S., Schmid, B., Tinevez, J.-Y., White, D. J., Hartenstein, V., Eliceiri, K., Tomancak, P., and Cardona, A., 2012, “Fiji: An Open-Source Platform for Biological-Image Analysis,” *Nature Methods*, **9**, p. 676.
- [25] Dressler, A. D., Jost, E. W., Miers, J. C., Moore, D. G., Seepersad, C. C., and Boyce, B. L., 2019, “Heterogeneities Dominate Mechanical Performance of Additively Manufactured Metal Lattice Struts,” *Additive Manufacturing*, **28**, pp. 692–703.
- [26] “ASM Material Data Sheet” [Online]. Available: <http://asm.matweb.com/search/SpecificMaterial.asp?bassnum=MQ316Q>. [Accessed: 10-Jun-2019].